Negative Refraction in Mechanical Rotator Lattices

Lezheng Fang and Michael J. Leamy*

School of Mechanical Engineering, Georgia Institute of Technology, Atlanta, Georgia 30332, USA

(Received 31 August 2022; revised 10 November 2022; accepted 22 November 2022; published 20 December 2022)

This paper presents numerical and experimental investigations of negative refraction at the interface between two mechanical rotator lattices, adding to the recent body of anomalous wave behavior reported for such simple lattices. Each lattice implements easily reconfigured interrotator coupling which determines whether the lattice's passband is acoustic (with positive group velocity) or optic (with negative group velocity). Since the group velocities have opposite signs over the entirety of both lattices' Brillouin zones, the negative refraction at their interface is inherently broadband. The numerical study constructs a large lattice structure for full-wave simulation and quantitatively analyzes the linear and nonlinear negative refraction. The experimental study documents robust negative refraction in a smaller-scale fabricated system and serves as validation for the numerical findings. We observe frequency-dependent transmission in both simulations and experiments. A linear analysis captures the observed phenomenon at low amplitude. At larger amplitudes, numerical simulations are used to document amplitude-dependent transmission. This phenomenon is explained by a nonlinear dispersion shift and transitional evanescent waves analyzed using a perturbation method. A sensitivity test demonstrates the robustness of negative refraction in the proposed rotator lattice structure.

DOI: 10.1103/PhysRevApplied.18.064058

I. INTRODUCTION

Negative refraction describes an anomalous wave phenomenon wherein the refraction of an oblique incident wave occurs on the same side as the interface normal, which can be compared to conventional materials wherein refraction occurs on the opposite side. The concept was first predicted by V. Veselago [1], who developed a theory of left-handed optical materials with simultaneous negative permittivity and permeability. Later, Pendry [2] showed that negative refractive index materials improve the imaging resolution beyond the diffraction limit. This extraordinary property motivated further exploration into subwavelength focusing [2–4], superlens imaging [5–7], waveguiding [8–10], and fabrication of negative index materials [11,12].

Negative refraction is not peculiar to electromagnetic waves. Recent studies have demonstrated analogous phenomena in acoustics (including phononics) [13,14]. Typically, an acoustic negative refractive index material requires negative effective mass density and bulk modulus at the operating frequency [15] or metamaterial designs with the passband's group velocity antiparallel to the wavevector. Such band structures can result from (i) resonance-based periodic structures [16–19], (ii) hyperbolic metamaterials [20,21], (iii) space coiling metamaterials [22–26], and perforated and pillared phononic crystals [27–30]. Practical implementations of the resonating mechanism usually consider Helmholtz resonators [16] for fluid-borne sound and hollow microstructures [19] for elastic waves. Due to the nature of resonance, these materials suffer from narrow operating ranges. Alternative designs consider folded acoustic channels [22,24] or extreme anisotropic structures [20] to generate negative refractive index passbands. These designs broaden the operating frequency range to some extent, but are restricted by intricate unit cell designs or only allow for partial focusing. In addition, the analysis of acoustic and elastic negative refraction remains largely devoted to the linear regime. The nonlinear effect of negative refraction, such as associated with amplitude-dependent dispersion, has been formulated in optics [31], yet sparsely investigated in acoustics.

In this study, we numerically and experimentally investigate negative refraction in a reconfigurable nonlinear rotator lattice. Such rotator lattice structures support a number of anomalous wave behaviors, including nonreciprocity [32] and dispersion morphing [33]. Different from other metamaterials harnessing the gyroscopic effects [34–37] and temporal modulation [38] of rotating units, the proposed two-dimensional (2D) lattice structure leverages the in-plane rotational geometry to determine the sign of the refractive index and also yields geometric nonlinearity (Sec. II). At the interface between two lattices with opposite-sign refractive indices, we observe robust negative refraction in numerical simulations (Sec. III)

---

*michael.leamy@me.gatech.edu

and experiments (Sec. IV). Linear dispersion analysis and perturbation-based nonlinear analysis respectively reveal the frequency and amplitude dependence of the refraction transmission, and predict an amplitude saturation effect. The experiment demonstrates the predicted negative refraction in a finite lattice. We also present a sensitivity study to quantify the robustness of the phenomenon in the experimental setup. These results improve the understanding of negative refraction in the presence of nonlinearity and suggest a promising design for future wave-based devices.

II. LATTICE DESIGN

Figures 1(a) and 1(b) depict two monatomic rotator lattices with alternate coupling arrangements. In both configurations, the rotators are pinned at their centers such that only angular oscillations occur. We define the counterclockwise rotation to be positive. In Fig. 1(a), each pair of adjacent rotators is connected by two linear elastic linkages mounted on their side arms. As such, we term this type of lattice the side-arm (SA) connected lattice. In Fig. 1(b), however, the adjacent rotators are linked from their nearest arm by only one lightly prestretched elastic linkage, and this type of lattice is termed the nearest-arm (NA) connected lattice.

Figures 1(c) and 1(d) provide detailed views of the SA and NA connections, respectively. To describe the dynamics, we introduce the system parameters: the rotator radius r, lattice constant a, gap distance $D = a - 2r$, spring stiffness k_{SA} and k_{NA}, and undeformed length L_0^{SA} and L_0^{NA}. When the lattice is perturbed, the elastic linkages between two adjacent rotators are deformed and produce restoring torques. In Fig. 1(c), the restoring torque at the rotator of interest (the left rotator) is the sum of the torques from the top and bottom elastic linkages connecting to its neighbor (the right rotator),

$$\mathbf{T}_{\mathrm{SA}} = \mathbf{r}_{\mathrm{top}}^{\mathrm{SA}} \times (k_{\mathrm{SA}}\delta\mathbf{L}_{\mathrm{top}}) + \mathbf{r}_{\mathrm{bot}}^{\mathrm{SA}} \times (k_{\mathrm{SA}}\delta\mathbf{L}_{\mathrm{bot}}), \tag{1}$$

where the radius vectors (parallel to the connecting arm), $\mathbf{r}_{\mathrm{top}}^{\mathrm{SA}}$, $\mathbf{r}_{\mathrm{bot}}^{\mathrm{SA}}$, and the deformation vectors (parallel to the elastic linkage), $\mathbf{L}_{\mathrm{top}}$ and $\mathbf{L}_{\mathrm{bot}}$, are derived from the rotational geometry,

$$\mathbf{r}_{\mathrm{top}}^{\mathrm{SA}} = \begin{bmatrix} r\cos\left(\theta_i + \frac{\pi}{2}\right) \\ r\sin\left(\theta_i + \frac{\pi}{2}\right) \end{bmatrix},$$

$$\mathbf{r}_{\mathrm{bot}}^{\mathrm{SA}} = \begin{bmatrix} r\cos\left(\theta_i - \frac{\pi}{2}\right) \\ r\sin\left(\theta_i - \frac{\pi}{2}\right) \end{bmatrix},$$

$$\delta\mathbf{L}_{\mathrm{top}} = (|\mathbf{L}_{\mathrm{top}}| - L_0^{\mathrm{SA}})\frac{\mathbf{L}_{\mathrm{top}}}{|\mathbf{L}_{\mathrm{top}}|},$$

$$\delta\mathbf{L}_{\mathrm{bot}} = (|\mathbf{L}_{\mathrm{bot}}| - L_0^{\mathrm{SA}})\frac{\mathbf{L}_{\mathrm{bot}}}{|\mathbf{L}_{\mathrm{bot}}|},$$

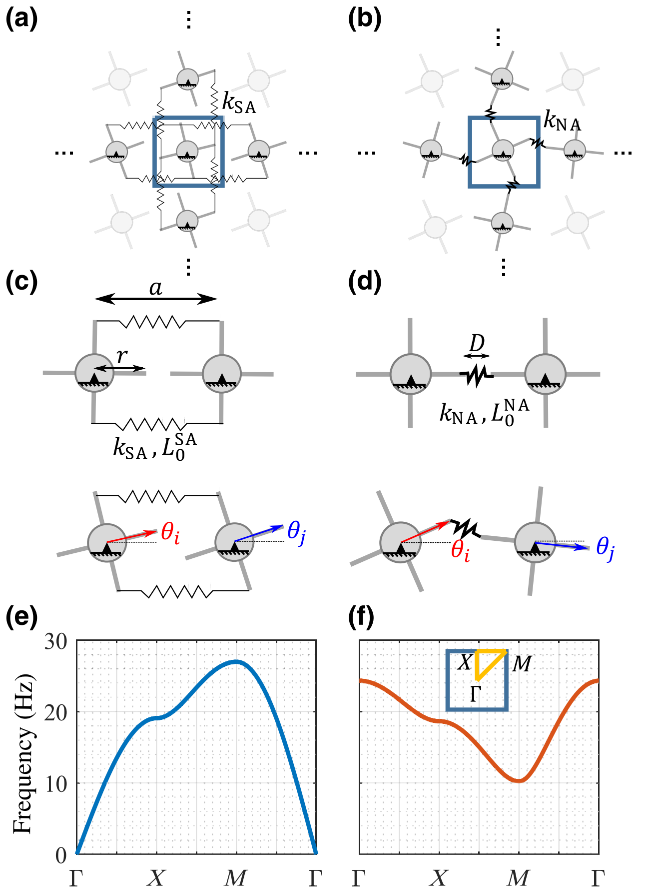

FIG. 1. Schematics of SA type (a) and NA type (b) rotator lattice structures. The blue square identifies the unit cell. (c) Detailed view of the SA inter-rotator connection. (d) Detailed view of the NA inter-rotator connection. (e) SA lattice linear dispersion relation. (f) NA lattice linear dispersion relation.

$$\mathbf{L}_{\mathrm{top}} = \begin{bmatrix} a + r\cos\left(\theta_j + \frac{\pi}{2}\right) - r\cos\left(\theta_i + \frac{\pi}{2}\right) \\ r\sin\left(\theta_j + \frac{\pi}{2}\right) - r\sin\left(\theta_i + \frac{\pi}{2}\right) \end{bmatrix},$$

$$\mathbf{L}_{\mathrm{bot}} = \begin{bmatrix} a + r\cos\left(\theta_j - \frac{\pi}{2}\right) - r\cos\left(\theta_i - \frac{\pi}{2}\right) \\ r\sin\left(\theta_j - \frac{\pi}{2}\right) - r\sin\left(\theta_i - \frac{\pi}{2}\right) \end{bmatrix}, \tag{2}$$

For the NA lattice, the restoring torque arises from the spring connecting the nearest arms of a pair of neighboring rotators,

$$\mathbf{T}^{\mathrm{NA}} = \mathbf{r}^{\mathrm{NA}} \times (k_{\mathrm{NA}}\delta\mathbf{L}_{\mathrm{mid}}), \tag{3}$$

where the radius and deformation vectors are provided by

$$\mathbf{r}^{\mathrm{NA}} = \begin{bmatrix} r\cos(\theta_i) \\ r\sin(\theta_i) \end{bmatrix},$$

$$\delta\mathbf{L}_{\mathrm{mid}} = (|\mathbf{L}_{\mathrm{mid}}| - L_0^{\mathrm{NA}})\frac{\mathbf{L}_{\mathrm{mid}}}{|\mathbf{L}_{\mathrm{mid}}|},$$

$$\mathbf{L}_{\mathrm{mid}} = \begin{bmatrix} a - r\cos(\theta_j) - r\cos(\theta_i) \\ -r\sin(\theta_j) - r\sin(\theta_i) \end{bmatrix}. \tag{4}$$

Accordingly, we derive the equation of motion governing the dynamics in both SA and NA lattices. The exact equations are, however, cumbersome due to the rotational geometry. In this study, we confine our attention to small-angle (wave-amplitude) motions, and Taylor-expand the equations of motion around the equilibrium position of the rotators. As such, we present the equations of motion for the SA and NA lattice, respectively:

$$\begin{aligned} I_{\mathrm{SA}}\ddot{\theta}_{m,n} &+ \epsilon\sum_{p,q} k_1(\theta_{m,n}-\theta_{p,q}) \\ &+ \epsilon^3\sum_{p,q}(\gamma_+^{\mathrm{SA}}(\theta_{m,n}+\theta_{p,q})^3+\gamma_-^{\mathrm{SA}}(\theta_{m,n}-\theta_{p,q})^3 \\ &+ \gamma_g^{\mathrm{SA}}\theta_{m,n}^3) + O(\epsilon^5) = 0, \qquad (5) \end{aligned}$$

$$\begin{aligned} I_{\mathrm{NA}}\ddot{\theta}_{m,n} &+ \epsilon\sum_{p,q}(k_2(\theta_{m,n}-\theta_{p,q})+k_g\theta_{m,n}) \\ &+ \epsilon^3\sum_{p,q}(\gamma_+^{\mathrm{NA}}(\theta_{m,n}+\theta_{p,q})^3+\gamma_-^{\mathrm{NA}}(\theta_{m,n}-\theta_{p,q})^3 \\ &+ \gamma_g^{\mathrm{NA}}\theta_{m,n}^3) + O(\epsilon^5) = 0, \qquad (6) \end{aligned}$$

where I and θ denote rotational inertia and angular displacement, respectively. Subscripts $[m,n]$ define the coordinates of the rotator of interest in the 2D lattice, and $[p,q] \in \{[m-1,n],[m+1,n],[m,n-1],[m,n+1]\}$ defines the neighbors of the $[m,n]$ rotator. The linear stiffnesses k_1, k_2, k_g and nonlinear stiffness γ_+, γ_-, γ_g are functions of the physical spring stiffnesses k_{SA} and k_{NA}, as well as the rotational geometry defined by rotator radius r and lattice constant a. We provide the explicit expressions for these equivalent stiffness functions in Appendix A. In both equations, the small parameter ϵ serves as a bookkeeping device in the series expansion and can be set to 1 in numerical evaluations. We present a set of experimentally measured parameters in Table I.

Next, we investigate linear and weakly nonlinear wave propagation. In both scenarios, the linear dispersion serves as important guidance for direct analysis and nonlinear corrections. With all nonlinear terms omitted, we present the linearized equations of motion and derive the linear dispersion relations [39],

$$I_{\mathrm{SA}}\ddot{\theta}_{m,n} + \sum_{p,q} k_1(\theta_{m,n}-\theta_{p,q}) = 0, \qquad (7)$$

$$\omega = \sqrt{\frac{k_1(4-2\cos(\mu_x)-2\cos(\mu_y))}{I_{\mathrm{SA}}}}, \qquad (8)$$

$$I_{\mathrm{NA}}\ddot{\theta}_{m,n} + \sum_{p,q}(k_2(\theta_{m,n}-\theta_{p,q})+k_g\theta_{m,n}) = 0, \qquad (9)$$

$$\omega = \sqrt{\frac{4k_g + k_2(4+2\cos(\mu_x)+2\cos(\mu_y))}{I_{\mathrm{NA}}}}, \qquad (10)$$

where μ_x, μ_y, and ω represent the wavenumber components along lattice directions, and the angular frequency, respectively.

For the SA lattice, Eq. (7) describes lattice dynamics identical to a conventional rectilinear 2D monatomic lattice, and Eq. (8) suggests an acoustic branch, depicted in Fig. 1(e). The NA lattice, on the other hand, contains an anomalous stiffness term in Eq. (9), the sum of adjacent rotators' displacement in contrast to the difference commonly seen in rectilinear lattices. This nuance gives rise to optical dispersion captured by Eq. (10) and depicted in Fig. 1(f). The difference in group velocity sign, over the entire Brillouin zone of each lattice, leads to broadband negative refraction at the interface joining the two lattice types.

To investigate the negative refraction, we layer the SA and NA lattices as shown in Fig. 2(a), and consider an oblique incident wave for the interface problem. We purposefully choose a small frequency range over which the incident and receiving medium exhibit spatial beaming behavior such that visual inspection leads to clear evidence of negative refraction in a finite-sized lattice.

TABLE I. Experimentally measured system parameters.

Parameter	I_{SA} (kg m^2)	I_{NA}	k_1 (N m)	k_2	k_g
Value	1.95×10^{-5}	4.05×10^{-5}	0.070	0.097	0.042
Parameter	γ_+^{SA} (N m)	γ_-^{SA}	γ_g^{SA}		
Value	5.1×10^{-3}	-6.6×10^{-3}	-0.0406		
Parameter	γ_+^{NA} (N m)	γ_-^{NA}	γ_g^{NA}		
Value	2.407	-0.011	1.1815		

III. ANALYSIS AND SIMULATION

We next present linear and nonlinear analyses of the negative refraction and its transmission. The numerical study considers a 90 × 90 rotator lattice split into two domains: the incident SA lattice and receiving NA lattice. The simulations are conducted in MATLAB by directly integrating the governing equations of motion, Eqs. (5) and (6), via the MATLAB function ode45. We assume the lattice is sufficiently large that the reflections from boundaries do not interfere with the refraction pattern near the interface in the simulation time window considered.

A. Linear Analysis and Simulation

As shown in Fig. 2(a), a 45-degree incident wave with frequency $f = 17$ Hz and small amplitude $A = 0.01$ rad transmits through the interface and refracts on the same side as the normal. At this small wave amplitude, the

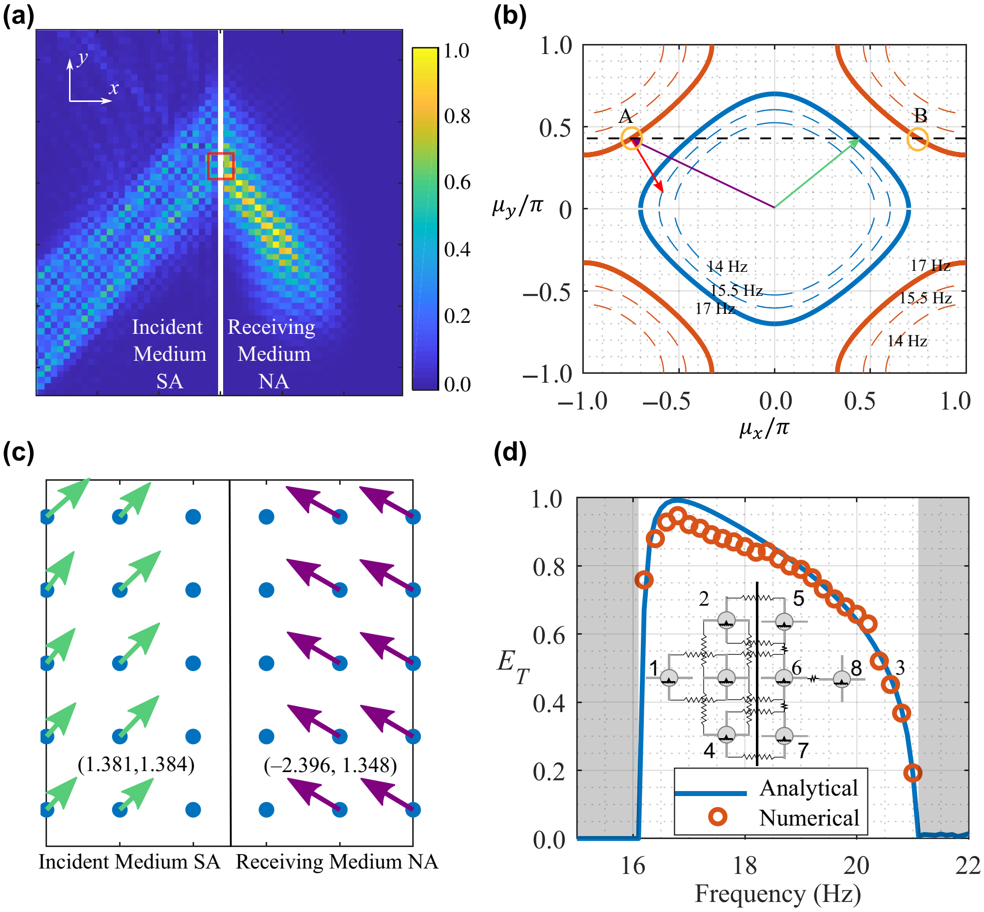

FIG. 2. Linear analysis and simulation of interfacing lattice structures. (a) Numerical demonstration of negative refraction at signal frequency $f = 17$ Hz, and amplitude $A = 0.01$ rad. Each pixel denotes the normalized energy at an individual rotator. (b) The isofrequency contours of the SA-type (blue) and NA-type (red) lattices. The contours at signal frequency ($f = 17$ Hz) are highlighted using solid lines. Dashed contours denote lower frequencies. (c) Numerically measured wavevectors at highlighted region in (a). The averaged wavenumber in each medium is numerically evaluated and presented in the form of (μ_x, μ_y). (d) The analytical and numerical energy transmission. The schematic of a control volume model to study transmission is embedded in the center. Rotators 1, 2, 3, 4 belong to the incident medium, and 5, 6, 7, 8 the receiving medium.

nonlinear effects are negligible. Since both media are anisotropic and dispersive, a powerful tool to investigate the refraction is the isofrequency contours plot derived from the linear dispersion, Eqs. (8) and (10).

Figure 2(b) displays the isofrequency contours, where the blue and red solid curves indicate the isofrequency contour at the signal frequency for the SA lattice (incident medium) and the NA lattice (receiving medium), respectively. Two lower frequency contours are also displayed as dashed curves, suggesting outward group velocity (gradient of the frequency contour) for the incident medium (SA) and inward group velocity for the receiving medium (NA). The green arrow depicts the incident wavevector. At the interface, the tangential wavenumber (μ_y) remains unchanged due to momentum conservation, and the refracted wavevector is thus constrained to fall along the black dashed line. The black dashed line intersects the isofrequency contour of the receiving medium at two points, A and B. To enable a positive energy inlet for the receiving medium, the refracted wavevector (purple arrow) is directed from the origin to point A since the group velocity (red arrow) has a positive component in the horizontal direction. We note that the group velocity and wavevector at this point assume roughly opposite directions in the receiving medium. This counterintuitive result is numerically verified in Fig. 2(c). The green and purple arrows depict incident and refracted wavevectors measured at each rotator (blue dot). The wavenumbers are computed via the phase-difference method [40] using adjacent rotators' responses. Note that this method assumes periodicity around the rotator considered, which does not apply to the rotators at the center two columns.

Due to the dispersive nature of the medium, the transmission is frequency-dependent. We quantitatively derive this frequency dependence by matching two plane wave solutions at the interface. A control volume straddling the interface is illustrated in Fig. 2(d), where four rotators are displayed on each side of the interface. The steady-state solutions for the rotators are informed by the dispersion relations in either medium and the force balance at the interface. With the dispersion relation established in Eqs. (8) and (10), we provide the force-balance equations at rotators 3 and 6 straddling the interface:

$$\begin{aligned}
&-\omega^2 I_{\mathrm{SA}}\theta_3 + k_1(\theta_3-\theta_1) + k_1(\theta_3-\theta_2)\\
&\quad + k_1(\theta_3-\theta_4) + k_1(\theta_3-\theta_6) = 0, \qquad (11)\\
&-\omega^2 I_{\mathrm{NA}}\theta_6 + k_1(\theta_6-\theta_3) + (k_g\theta_6 + k_2(\theta_6+\theta_5))\\
&\quad (k_g\theta_6 + k_2(\theta_6+\theta_7)) + (k_g\theta_6 + k_2(\theta_6+\theta_8)) = 0. \qquad (12)
\end{aligned}$$

By introducing the wave amplitude A, complex transmission T, and reflection coefficient R, we can describe the steady-state response of each rotator θ_i in Table II. Substituting these assumed wave solutions back into Eqs. (11) and (12), we obtain two algebraic equations in two unknowns, T and R. Note that the wavevectors for the incident and receiving medium, $[\mu_x^{\mathrm{SA}}, \mu_y^{\mathrm{SA}}]$ and $[\mu_x^{\mathrm{NA}}, \mu_y^{\mathrm{NA}}]$, can be derived from the dispersion analysis presented in Fig. 2(b), given incident wave angle and frequency. In Fig. 2(d), we illustrate the frequency-dependent transmission from an energy perspective, $E_T = 1 - |R|^2$. The dome-shaped transmission peaks at approximately $f = 16.75$ Hz, indicating an impedance matching between two lattices. Similar to the specific acoustic impedance, the specific elastic impedance in a discrete lattice can be formulated as pressure (torque) over particle (rotator) velocity, P/v (or T/ω). We note that the torque T is provided by either the horizontal or vertical elastic linkages. Thus the impedance in each direction needs to be considered individually. Assuming plane wave propagation $e^{i(\omega t - \mu_x x - \mu_y y)}$, with angle $\phi = \mathrm{atan}(\mu_y/\mu_x)$, we derive the specific elastic impedance $\mathbf{z}$ for the SA and NA lattices in each lattice direction, respectively:

$$\begin{aligned}
\mathbf{z}_{\mathrm{SA}.x}(\omega,\phi) &= -\frac{k_1(1-e^{i\mu_x^{\mathrm{SA}}(\omega,\phi)})}{i\omega},\\
\mathbf{z}_{\mathrm{SA}.y}(\omega,\phi) &= -\frac{k_1(1-e^{i\mu_y^{\mathrm{SA}}(\omega,\phi)})}{i\omega}, \qquad (13)\\
\mathbf{z}_{\mathrm{NA}.x}(\omega,\phi) &= -\frac{k_g + k_2(1+e^{i\mu_x^{\mathrm{NA}}(\omega,\phi)})}{i\omega},\\
\mathbf{z}_{\mathrm{NA}.y}(\omega,\phi) &= -\frac{k_g + k_2(1+e^{i\mu_y^{\mathrm{NA}}(\omega,\phi)})}{i\omega}, \qquad (14)
\end{aligned}$$

where $[\mu_x^{\mathrm{SA}}, \mu_y^{\mathrm{SA}}]$ and $[\mu_x^{\mathrm{NA}}, \mu_y^{\mathrm{NA}}]$ are dimensionless wavenumber functions of frequency ω and wave angle ϕ. The SA lattice impedance described by Eq. (13) can be further simplified to $\mathbf{z}_k = \sqrt{k_1 m} e^{i\frac{\mu_k}{2}}$ ($k = x$ or y) using the dispersion relationship, agreeing with [41]. We note that the specific impedance in discrete lattices is naturally complex. In the long-wavelength limit, this expression approaches $\mathbf{z} = \sqrt{k_1 m}$, recovering the elastic characteristic impedance.

TABLE II. Assumed solutions in the interface model.

Rotator	Expression
θ_1	$Ae^{-i\omega t}e^{-i\mu_x^{\mathrm{SA}}} + R \times Ae^{-i\omega t}e^{i\mu_x^{\mathrm{SA}}}$
θ_2	$Ae^{-i\omega t}e^{i\mu_y^{\mathrm{SA}}} + R \times Ae^{-i\omega t}e^{i\mu_y^{\mathrm{SA}}}$
θ_3	$Ae^{-i\omega t} + R \times Ae^{-i\omega t}$
θ_4	$Ae^{-i\omega t}e^{-i\mu_y^{\mathrm{SA}}} + R \times Ae^{-i\omega t}e^{-i\mu_y^{\mathrm{SA}}}$
θ_5	$T \times Ae^{-i\omega t}e^{i\mu_y^{\mathrm{NA}}}$
θ_6	$T \times Ae^{-i\omega t}$
θ_7	$T \times Ae^{-i\omega t}e^{-i\mu_y^{\mathrm{NA}}}$
θ_8	$T \times Ae^{-i\omega t}e^{i\mu_x^{\mathrm{NA}}}$

Since the interface is vertically placed (two media connected horizontally), a full transmission implies horizontal impedance matching,

$$\begin{aligned}
|\mathbf{z}_{\mathrm{SA}.x}(\omega,\phi_i)| &= |\mathbf{z}_{\mathrm{NA}.x}(\omega,\phi_r)|,\\
|k_1(1-e^{i\mu_x^{\mathrm{SA}}(\omega,\phi_i)})| &= |k_g + k_2(1+e^{i\mu_x^{\mathrm{NA}}(\omega,\phi_r)})|, \qquad (15)
\end{aligned}$$

where ϕ_i and ϕ_r denote the incident wave angle and refracted wave angle respectively. For the 45° incident wave considered, this equation yields $\omega = 16.75$ Hz $\times\, 2\pi$ as the impedance matching frequency, agreeing with the observation in Fig. 2(d).

The gray regions in Fig. 2(d) ($f < 16$ Hz and $f > 21$ Hz) indicate complex wavenumbers in the receiving medium, and trivial transmission in the far field. From the isofrequency contour perspective, this suggests no intersection between the black dashed line and the red contours in Fig. 2(b). This operation range is narrower than the common passband range of the incident and receiving medium, as indicated in Figs. 1(e) and 1(f) (approximately 10–24 Hz). We note that the common passband in Figs. 1(e) and 1(f) accounts for wave propagation in all possible directions, while the narrower common passband in Fig. 2(d) corresponds to a 45° incident wave only. As this specific angle, the operation range is naturally narrower, as also indicated in the isofrequency contours in Fig. 2(b). Finally, the analytical transmission curve quantitatively agrees with the observation in the numerical simulation.

B. Nonlinear Transmission

We next explore the refraction at higher amplitudes where nonlinear effects emerge. Figures 3(a) and 3(b) depict such a scenario: at incident wave amplitudes $A = 0.08$ rad and $A = 0.16$ rad, the increasing wave amplitude decreases the transmission. Figure 3(c) compares the time responses at the same rotator in the receiving field under different incident amplitudes. The results indicate the receiving amplitudes are approximately equal, though their incident amplitudes differ by a factor of 2.

Tracing the time responses of rotators along the transmission path, we plot the spatial evolution of the wave amplitude in Fig. 3(d) under different incident amplitudes. At low amplitudes, the transmitted waves maintain their amplitudes along the transmission line, agreeing with the linear theory. However, at higher amplitudes, an attenuation envelope emerges after the interface. It is noteworthy that, different from the attenuation envelope resultant from the linear bandgap effect, this attenuation envelope does not vanish in the far field, but rather saturates the amplitude. This unconventional behavior, together with amplitude-dependent transmission, can be explained via a perturbation analysis.

We use the method of multiple scales (MMS) to quantitatively describe the observed nonlinear effect [42,43]. Adhering to the MMS procedure [44], we introduce a small parameter ϵ as a bookkeeping device to define multiple time scales,

$$T_0 = t, T_1 = \epsilon t, T_n = \epsilon^n t. \tag{16}$$

Accordingly, the time derivatives now become

$$\begin{aligned}\dot{(\,)} &= D_0(\,) + \epsilon D_1(\,) + O(\epsilon^2),\\ \ddot{(\,)} &= D_0^2(\,) + 2\epsilon D_0 D_1(\,) + O(\epsilon^2),\end{aligned} \tag{17}$$

where D_n corresponds to the partial time derivative with respect to T_n. Similarly, we expand the wave response as an asymptotic series,

$$\theta_{m,n} = \theta_{m,n}^{(0)} + \epsilon\theta_{m,n}^{(1)} + O(\epsilon^2). \tag{18}$$

In Table I we notice the SA lattice has considerably smaller nonlinearity compared to the NA lattice. Hence, we deduce that the observed nonlinear effects mostly arise from the NA lattice nonlinearity. For simplicity, we treat the SA lattice as linear, and conduct MMS on the NA lattice.

Substituting Eqs. (17) and (18) into the NA lattice equation of motion [Eq. (6)], we collect terms at the first two orders,

$$O(\epsilon^0) : I_{\mathrm{NA}} D_0^2 \theta_{m,n}^{(0)} + \sum_{p,q}[k_g \theta_{m,n}^{(0)} + k_2(\theta_{m,n}^{(0)} + \theta_{p,q}^{(0)})] = 0, \tag{19}$$

$$\begin{aligned}O(\epsilon^1) : I_{\mathrm{NA}} D_0^2 \theta_{m,n}^{(1)} &+ \sum_{p,q}[k_g \theta_{m,n}^{(1)} + k_2(\theta_{m,n}^{(1)} + \theta_{p,q}^{(1)})]\\ &= -2ID_0D_1\theta_{m,n}^{(0)} - \sum_{p,q}[\gamma_+^{\mathrm{NA}}(\theta_{m,n}^{(0)} + \theta_{p,q}^{(0)})^3\\ &\quad + \gamma_-^{\mathrm{NA}}(\theta_{m,n}^{(0)} - \theta_{p,q}^{(0)})^3 + \gamma_g^{\mathrm{NA}}(\theta_{m,n}^{(0)})^3].\end{aligned} \tag{20}$$

The solution to Eq. (19) assumes the form of a 2D plane wave,

$$\theta_{m,n}^{(0)} = \frac{1}{2} C e^{i\omega_0 T_0} e^{-i\mu_x} e^{-i\mu_y} + \text{c.c.}, \tag{21}$$

where amplitude C is a complex quantity, and c.c. denotes the complex conjugate of the preceding terms. The dispersion relation of this zeroth-order solution takes the same form as in Eq. (10). In the implementation of MMS, we typically express the complex conjugate in its polar form to decouple the nonlinear effects on amplitude and phase at slower time scales:

$$\begin{aligned}\alpha &= \alpha(T_1, T_2, \ldots),\\ \beta &= \beta(T_1, T_2, \ldots),\\ C &= \alpha e^{i\beta}.\end{aligned} \tag{22}$$

Substituting the zeroth-order solution Eqs. (21) and (22) into the first-order expansion Eq. (20), we obtain a lengthy expression on the right-hand side (omitted here). This expression contains information to construct the first-order solution, yet needs to be modified due to the secular terms containing $e^{i\omega T_0} e^{-i\mu_x} e^{-i\mu_y}$ and their complex conjugates. Secular terms need to be removed to avoid unbounded growth violating the asymptotic expansion in Eq. (18). By separating and removing secular terms for the real and imaginary parts, we obtain two ordinary differential equations governing the slow evolution of α and β:

$$D_1 \alpha = 0, \tag{23}$$

$$\begin{aligned}D_1\beta = \frac{\alpha^2}{I_{\mathrm{NA}}\omega_0}\Bigg[&\frac{3}{2}\gamma_g^{\mathrm{NA}} + \frac{9}{2}(\gamma_-^{\mathrm{NA}} + \gamma_+^{\mathrm{NA}})\\ &- 3(\gamma_-^{\mathrm{NA}} - \gamma_+^{\mathrm{NA}})(\cos\mu_x + \cos\mu_y)\\ &+ \frac{3}{4}(\gamma_-^{\mathrm{NA}} + \gamma_+^{\mathrm{NA}})(\cos 2\mu_x + \cos 2\mu_y)\Bigg] = \delta\alpha^2.\end{aligned} \tag{24}$$

These results suggest that the wave amplitude α is not a function of the slow time T_1, and the phase β contributes to a frequency correction at the first order [42]:

$$\omega = \omega_0 + \epsilon\delta\alpha^2. \tag{25}$$

We present the nonlinear dispersion curves as isofrequency contours in Fig. 3(e) at a variety of wave amplitudes.

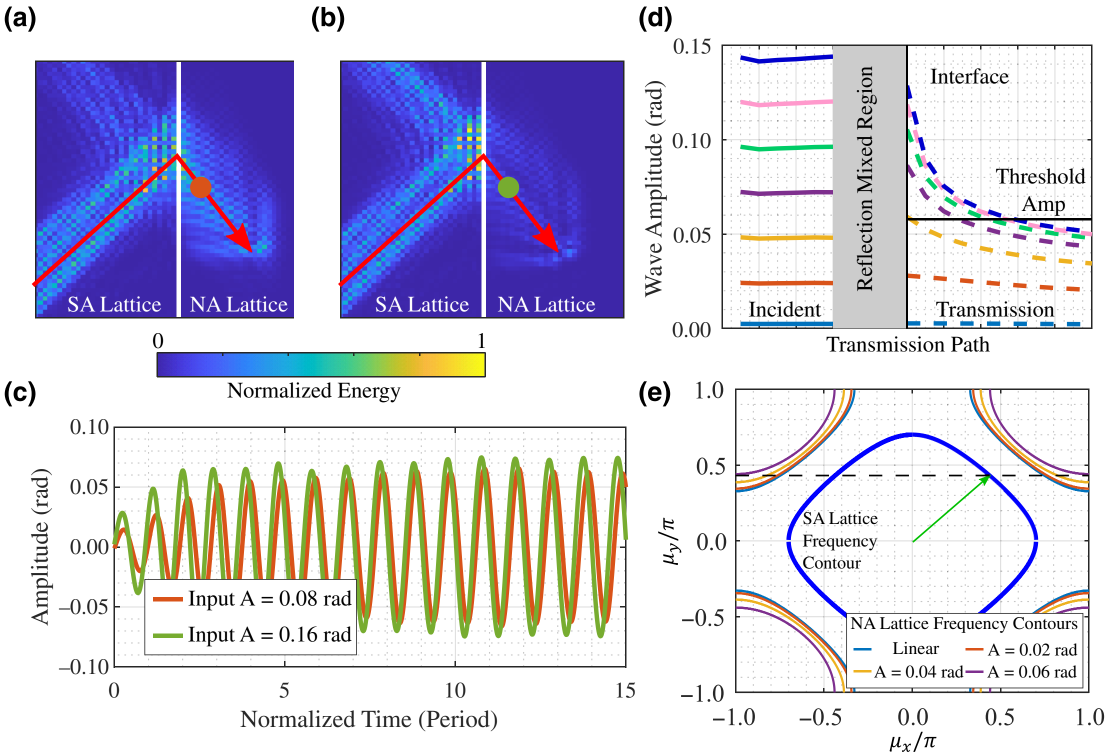

FIG. 3. (a) Wave propagation contour at amplitude $A = 0.08$ rad. The red arrow describes the transmission path considered. (b) Wave propagation contour at amplitude $A = 0.16$ rad. The pixelated energy in (a) and (b) is normalized between 0 and 1. (c) The transmitted signal at the same rotator [colored dots in (a) and (b)] of the lattice for excitation amplitudes $A = 0.08$ rad and $A = 0.16$ rad, respectively. The curve colors match the dot color in (a) and (b). (d) The amplitude envelope along the transmission path. Solid and dashed curves denote the incident and transmitted wave, respectively. (e) Amplitude-dependent isofrequency contours. The blue curve near the center refers to the isofrequency contour of the incident medium at the signal frequency. The groups of curves at corners mark the isofrequency contours of the receiving medium at linear (green), $A = 0$ rad (shallow blue), $A = 0.02$ rad (orange), $A = 0.04$ rad (yellow), $A = 0.06$ rad (purple). The green arrow denotes the incident wavevector. The black dashed line indicates the momentum conservation for μ_y.

Similar to Fig. 2(b), the blue contour at the center corresponds to the incident medium. It does not deform as the wave amplitude increases. The isofrequency contours for the receiving medium, however, migrate away towards the corners as the wave amplitude increases. Consider an incident signal denoted by the green arrow in Fig. 3(e). The refracted wave maintains the tangential wavevector μ_y, indicated by the black dashed line, which intersects the amplitude-dependent dispersion of the receiving medium at a nonlinear-shifted μ_x. As the amplitude increases, the black dashed line intersects the isofrequency contour of the receiving medium at a distant point, resulting in a larger difference in the phase velocity between the two media. From an impedance perspective, given unchanged inertia or density the enlarging phase velocity difference leads to an enhanced impedance mismatch, reducing the effective transmission.

If the amplitude is sufficiently large (e.g., the purple curve at $A = 0.06$ rad in Fig. 3), the black dashed line no longer intersects the isofrequency contour. As a result, the wavenumber along the normal, μ_x, becomes complex. In contrast to the linear theory, the nonlinear evanescent wave does not decay to zero, but rather saturates the amplitude below a threshold value, as observed in Fig. 3(d).

This behavior of nonlinear evanescent waves is analyzed theoretically in [45]. Typically, the nonlinear dispersion shift enables nonlinear passband extension (NPE) or nonlinear stopband extension (NSE), in which a propagating signal becomes a transitional evanescent wave featuring the saturation effect. In the NA-type lattice, the signal considered falls in the passband of the receiving medium at low amplitudes (the black dashed line intersects with the isofrequency contour), but falls in the stopband at high amplitudes (no intersection between black dashed line and the isofrequency contour), which meets the definition of a NSE. Just past the interface, the transmitted wave has high amplitude, which shifts the dispersion curves, and the signal falls in the stopband. As the amplitude decreases in transmission due to the bandgap effect, the nonlinear effect also mitigates. As pertains to the isofrequency contours, the shift lessens and the contour tends to migrate from the largest-amplitude position (purple) back to a lower-amplitude position (e.g., yellow). At a threshold amplitude wherein the black dashed line intersects the isofrequency contour, the amplitude attenuation ends, and the wave may propagate at a lower amplitude. As such, the lattice serves as an effective amplitude saturator. The saturation threshold can be determined from Eq. (25):

$$A_{\mathrm{sat}}(\omega, \mu_y) = \sqrt{\frac{\omega - \omega_0(\mu_x = \pi, \mu_y)}{\delta(\mu_x = \pi, \mu_y)}}. \qquad (26)$$

This quantity is a function of frequency ω, and incident wavenumber μ_y. It has a numerical value of 0.058 rad in this study. Noteworthy, the saturation profile in Fig. 3(d) does not fully flatten in the far field due to a wavenumber clipping effect [45,46].

IV. EXPERIMENT

This section presents an experimental study of the negative refraction at the interface of two fabricated rotator lattices. Due to the presence of dissipation and finite size, this study focuses on verifying linear negative refraction.

Figure 4(a) depicts the schematic of the experimental system—a matrix of 10 × 10 rotators (0.66 × 0.66 m) with the left five columns forming a SA lattice and the right five an NA lattice. In each lattice, 3D-printed rotators sit on low-friction bearings that are press-fit on fixed shafts. The distances between adjacent shafts are identical, $a = 0.068$ m. The rotators adopt a multilayer structure, allowing spring connections in both lattice directions. As depicted in the 3D illustrations in Fig. 4(a), the long springs (k_1) in the SA lattice rotator (the light blue rotator on the left) are pinned at different layers of the rotator such that the spring coils do not interfere. For the NA lattice rotator (the light red rotator on the right), the short springs (k_2) are all pinned at the same height. The rotator design also supports the installation of additional weights (screws and nuts) on the circular plate to tune the moment of inertia. In the experiment, we consider 5 pairs of screws and nuts for each SA lattice rotator and 12 screws and 48 nuts for each NA lattice rotator. This procedure enables a common passband between the two lattices, given a limited variety of extension springs, and minimizes the damping effect on the wave propagation.

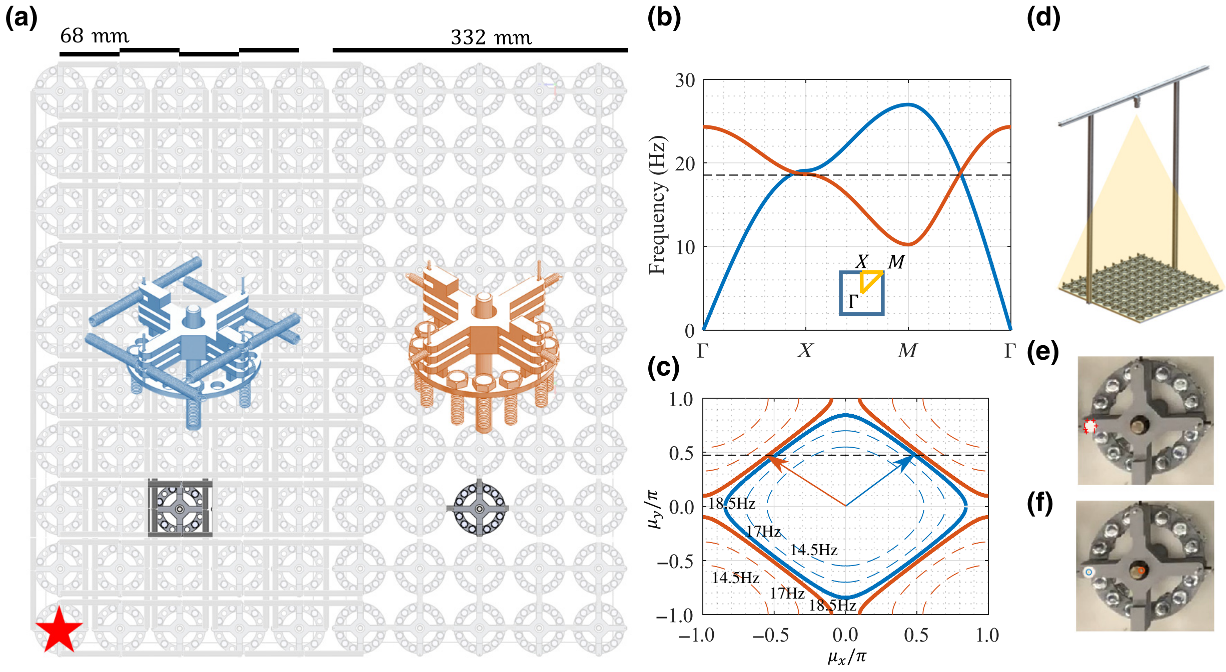

FIG. 4. (a) Schematic of the lattice interface system. The left five columns represent the SA-type connected rotator lattice (blue), while the right five columns represent the NA-type rotator lattice (red). The red star at the bottom left denotes the excitation position. The scale bar at top left marks the size of the experimental unit cell, and at top right the depth of each medium. (b) The dispersion relation of two lattices. Blue denotes the SA-type and red the NA-type. (c) The isofrequency contours of the SA-type (blue) and NA-type (red) rotator lattices near the excitation frequency 18.5 Hz, highlighted in thick solid curves. A pair of incident and refracted wavevectors are illustrated. (d) The schematic of the experimental setup with an elevated camera. (e) A frame of an individual rotator with red crosses marking the feature (reflection tape). (f) Illustration of the tracking point (blue) and the rotator center (red).

We use a single shaker (Brüel & Kjær 4810) to excite a continuous incident wave by prescribing the motion of the rotator at the bottom left corner, highlighted by the red star in Fig. 4. At a frequency of approximately 18.5 Hz [indicated as the dashed line in Fig. 4(b)], the isofrequency contour admits a rounded parallelogram shape [the blue solid contour in Fig. 4(c)]. Since the group velocity is always perpendicular to the isofrequency contour, the point excitation at the frequency induces a strong wave-beaming effect along 45° towards the interface [39]. Due to the nature of the single point source, the incident wave contains a mixture of wavevectors despite its highly directed energy flow. The mixed wavevectors affect the refraction transmission, yet do not alter the negative refraction pattern.

Upon excitation, the wave travels to the interface and splits into refracted and reflected components. This process is recorded by a high-speed camera positioned 1.22 m above the lattice, as shown in Fig. 4(d). At such a height, we ensure the error from the perspective geometry is sufficiently small. The camera records at 60 fps with 3840 × 2160 pixel resolution covering the entire 100-rotator matrix.

The data extraction involves two steps: (i) tracking the feature points, and (ii) conversion into angular displacement and velocity. Figure 4(e) presents a rotator image cropped from a single frame of the recording. The feature points are covered by reflection tape and marked by red crosses. We use a Kanade-Lucas-Tomasi algorithm-based MATLAB function, PointTracker, to track the movement of

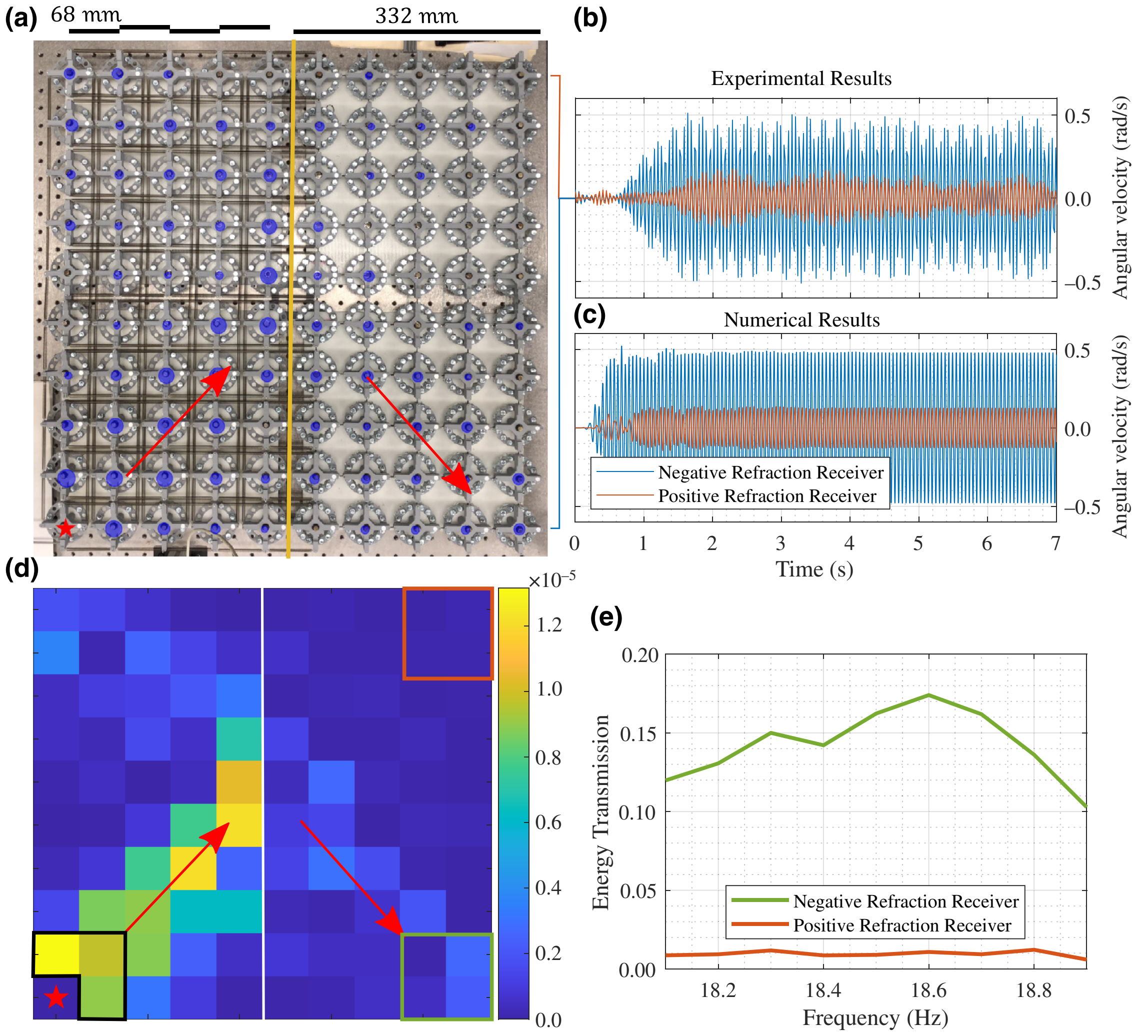

FIG. 5. (a) Single video frame from the experiment. The blue dot depicts the angular velocity of each rotator at the current frame. The orange line denotes the interface. (b) The experimental time response of the bottom right (blue) and the top right rotator (red). (c) The numerical time response of the same two rotators as in (b). (d) The experimental average kinetic energy at each rotator. (e) The experimental frequency-transmission relation for the negative refraction receiver and the positive refraction receiver.

the reflection tape for each individual rotator. By relating the position of the reflection tape (blue dot) to the center of the rotator (red dot), as illustrated in Fig. 4(f), we compute the angular displacement for each rotator and collectively monitor the global dynamics of the lattice. To remove small offsets on the angular displacement measurements, we present the results in terms of its time derivative (angular velocity) in Fig. 5.

Figure 5(a) depicts a video frame of the global dynamics, where the size of each blue dot is shown in proportion to the rotator's angular velocity. In the receiving medium, we observe most of the energy is refracted into the bottom right quarter, demonstrating negative refraction. Beyond this frame, we capture the full time history of the dynamics at the top right corner (positive refraction receiver), and bottom right corner (negative refraction receiver), and present them in Fig. 5(b). The response at the negative refraction receiver is approximately three times higher than that of the positive refraction receiver, providing quantitative evidence for negative refraction. We note that the positive refraction receiver has nontrivial readings due to the vibration of the finite structure, which is not seen in the Sec. III study. Accordingly, we numerically simulate the 10 × 10 experiment lattice with a point source placed at the bottom left corner and dissipation modeled as uniform viscous damping. The simulation result, which achieves a high degree of agreement with the experiment, is illustrated in Fig. 5(c).

From an energy perspective, the time-averaged kinetic energy in Fig. 5(d) reveals a more distinct pattern for the negative refraction. We identify the negatively refracted energy and positively refracted energy in the green and red square box, respectively. By comparing them to the source energy, which can be recognized from the black contour at bottom left, we quantify the energy transmission in Fig. 5(e). At the specified frequency range where directivity permits beaming incident waves, the negative refraction energy transmission is consistently higher than the positive refraction transmission. The frequency-dependent pattern deviates from the numerical prediction in Fig. 2(d) primarily due to the point source excitation and finite size of the lattice. The experimental transmission is lower than the theory due to dissipation and imperfect periodicity. We further evaluate the robustness of the observed negative refraction via a sensitivity study documented in Appendix B.

V. CONCLUDING REMARKS

We observe robust negative refraction between two simple rotator lattices in numerical simulations and experiments. The two proposed rotator lattices share a similar structure but have a subtle difference of spring attaching location. This variance configures the dispersion relation of the lattice to be either acoustic with positive group velocity or optic with negative group velocity. Since the group velocities have opposite signs over the entirety of both lattices' Brillouin zones, the negative refraction is inherently broadband. At low amplitude, a linear dispersion analysis illustrates the negative refraction mechanism, and demonstrates frequency-dependent transmission. The experimental results quantitatively agree with the numerical simulations. At higher amplitudes, perturbation analysis reveals amplitude-dependent transmission and a nonlinear saturation effect, verified in numerical simulations. A parameter sensitivity test indicates robust negative refraction in the rotator lattices with the presence of small imperfections.

ACKNOWLEDGMENTS

The authors would like to thank the National Science Foundation for support of this research under an Emerging Frontiers in Research and Innovation (EFRI) Grant No. 1741565. L.F. would like to thank Mr. Aryan Roy for his contributions to the rotator design.

APPENDIX A

This appendix presents the explicit expressions for linear and nonlinear stiffnesses as well as a brief introduction of the experimental parameter identification process.

Both SA and NA lattices have the same lattice constant a, and rotator radius r. Rotators in the SA lattice are connected via elastic linkages with stiffness k^{SA}, and undeformed length L_0^{SA}. The associated linear and nonlinear stiffnesses are given by

$$k_1 = 2k^{\mathrm{SA}}r^2, \tag{A1}$$

$$\gamma_+^{\mathrm{SA}} = \frac{k^{\mathrm{SA}}r^2L_0^{\mathrm{SA}}}{6a}, \tag{A2}$$

$$\gamma_-^{\mathrm{SA}} = \frac{k^{\mathrm{SA}}r^2(L_0^{\mathrm{SA}} - 2a)}{6a}, \tag{A3}$$

$$\gamma_g^{\mathrm{SA}} = -\frac{4k^{\mathrm{SA}}r^2L_0^{\mathrm{SA}}}{3a}. \tag{A4}$$

Rotators in the NA lattice are connected via elastic linkages with stiffness k^{NA}, and undeformed length L_0^{NA}. We introduce an edge-to-edge distance between two NA-connected rotators in the equilibrium position, $D = a - 2r$,

TABLE III. Experimentally identified system parameters.

Parameter	k_{SA} (N/m)	k_{NA}	L_0^{SA} (m)	L_0^{NA}
Value	39	820	0.0312	0.0012
Parameter	r (m)	a (m)		
Value	0.03	0.068		

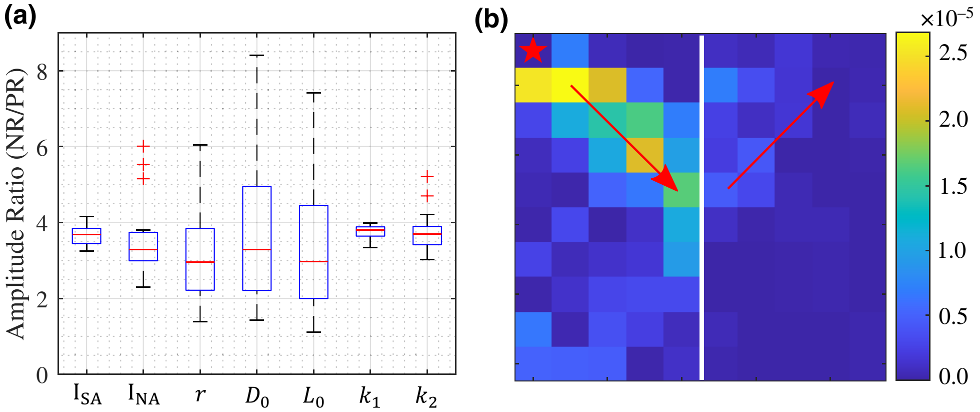

FIG. 6. (a) The sensitivity test for system parameters, shown as a boxplot. Twenty numerical simulations at small signal frequency $f = 18.5$ Hz are used for each parameter study. The vertical axis displays the amplitude ratio between the negative refraction receiver (NR) and the positive refraction receiver (PR). (b) The experimental results of the system excited from the top left corner instead of the bottom left. The average kinematic energy is plotted.

such that the stiffnesses are given by

$$k_2 = \frac{k_{NA} r^2 (D - L_0^{NA})}{D}, \tag{A5}$$

$$k_g = k_{NA} r (D - L_0^{NA}), \tag{A6}$$

$$\gamma_+^{NA} = \frac{k_{NA} r^2 L_0^{NA}}{2D}\left(\frac{r^2}{D^2} + \frac{5r}{6D} + \frac{1}{6}\right), \tag{A7}$$

$$\gamma_-^{NA} = \frac{k_{NA} r^2}{6}\left(1 - \frac{r L_0^{NA}}{2D} - \frac{L_0^{NA}}{2D}\right), \tag{A8}$$

$$\gamma_g^{NA} = \frac{k_{NA} r^2}{3}\left(\frac{2r^2 L_0^{NA}}{D^2} - r + \frac{L_0^{NA}}{D} - \frac{D - L_0^{NA}}{2}\right). \tag{A9}$$

The parameter identification process for NA and SA lattices is similar to the approach taken in our previous work [32]. By isolating each unit cell from the lattice, we experimentally measure its free oscillation response at different moments of inertia (controlled by adjusting the number of bolts and nuts) and energy levels. The collected results are fit to our analytical model, Eqs. (5) and (6), via the patternsearch function in MATLAB. In Table III, we also provide the average stiffnesses and undeformed lengths of the physical springs used in the experiments for reference.

APPENDIX B

To evaluate the robustness of the results, we assess the sensitivity of the negative refraction pattern subject to imperfect periodicity. In the numerical model of the 10 × 10 lattice, we introduce spatial randomness to the following parameters individually: rotator inertia (I_{SA} and I_{NA}), radius (r), spring spacing (D_0), short spring undeformed length (L_0), and spring stiffnesses (k_1 and k_2). The randomness is sampled from normal distributions with standard deviation equaling 2.5% of a parameter's expected value,

$$\{P\}_{N\times 1} \leftarrow \{\mathcal{N}(\overline{P}; (2.5\%\overline{P})^2)\}, \tag{B1}$$

where $\{P\}$ represents the vector of an arbitrary parameter, and N denotes the number of elements containing such parameter in the 10 × 10 lattice structure. For example, if the parameter of interest is the SA lattice rotator inertia, we have $P = I_{SA}$, and expected value $\overline{P} = 1.95E - 5$ kg m^2. There are 50 SA rotators in the system, so $N = 50$.

For each parameter sensitivity test, we consider 20 sets of spatial randomness sampled from Eq. (B1), and conduct simulations individually. We analyze the amplitude ratio between the negative refraction receiver and positive refraction receiver. The results are illustrated in the boxplot in Fig. 6(a). We observe that at the randomness level considered, the amplitude ratio is strictly larger than 1, implying a robust negative refraction. Additionally, the amplitude ratio is most sensitive to the geometric parameters r, D_0, and L_0. The variance resulting from spatial fluctuations on inertia and stiffness is small. The results connect the negative refraction performance to individual system parameters and suggest the significance of geometry resolution for designs and fabrications.

In addition to the parameter fluctuations, we provide an experimental result with varied excitation location (top left corner). Figure 6(b) depicts the results in terms of time-averaged kinetic energy. We observe a negative refraction pattern with refracted energy directed towards the top right, as expected.

[1] V. G. Veselago, Electrodynamics of substances with simultaneously negative values of ϵ and μ, Usp. Fiz. Nauk. **92,** 517 (1967).

[2] J. B. Pendry, Negative Refraction Makes a Perfect Lens, Phys. Rev. Lett. **85**, 3966 (2000).

[3] J. Pendry and S. A. Ramakrishna, Focusing light using negative refraction, J. Phys.: Condens. Matter **15**, 6345 (2003).

[4] A. Sukhovich, L. Jing, and J. H. Page, Negative refraction and focusing of ultrasound in two-dimensional phononic crystals, Phys. Rev. B **77**, 014301 (2008).

[5] P. V. Parimi, W. T. Lu, P. Vodo, and S. Sridhar, Imaging by flat lens using negative refraction, Nature **426**, 404 (2003).

[6] D. R. Smith, J. B. Pendry, and M. C. Wiltshire, Metamaterials and negative refractive index, Science **305**, 788 (2004).

[7] Z. Lu, S. Shi, C. A. Schuetz, and D. W. Prather, Experimental demonstration of negative refraction imaging in both amplitude and phase, Opt. Express **13**, 2007 (2005).

[8] A. Grbic and G. V. Eleftheriades, Experimental verification of backward-wave radiation from a negative refractive index metamaterial, J. Appl. Phys. **92**, 5930 (2002).

[9] F. Legrand, B. Gérardin, F. Bruno, J. Laurent, F. Lemoult, C. Prada, and A. Aubry, Cloaking, trapping and superlensing of lamb waves with negative refraction, Sci. Rep. **11**, 1 (2021).

[10] G. Bordiga, L. Cabras, A. Piccolroaz, and D. Bigoni, Prestress tuning of negative refraction and wave channeling from flexural sources, Appl. Phys. Lett. **114**, 041901 (2019).

[11] R. A. Shelby, D. R. Smith, and S. Schultz, Experimental verification of a negative index of refraction, science **292**, 77 (2001).

[12] W. J. Padilla, D. N. Basov, and D. R. Smith, Negative refractive index metamaterials, Mater. Today **9**, 28 (2006).

[13] X. Zhang and Z. Liu, Negative refraction of acoustic waves in two-dimensional phononic crystals, Appl. Phys. Lett. **85**, 341 (2004).

[14] R. V. Craster and S. Guenneau, *Acoustic Metamaterials: Negative Refraction, Imaging, Lensing and Cloaking* Vol. 166 (Springer, Dordrecht, 2012).

[15] J. Li and C. T. Chan, Double-negative acoustic metamaterial, Phys. Rev. E **70**, 055602(R) (2004).

[16] S. Zhang, L. Yin, and N. Fang, Focusing Ultrasound with an Acoustic Metamaterial Network, Phys. Rev. Lett. **102**, 194301 (2009).

[17] N. Kaina, F. Lemoult, M. Fink, and G. Lerosey, Negative refractive index and acoustic superlens from multiple scattering in single negative metamaterials, Nature **525**, 77 (2015).

[18] D. Tallarico, N. V. Movchan, A. B. Movchan, and D. J. Colquitt, Tilted resonators in a triangular elastic lattice: Chirality, Bloch waves and negative refraction, J. Mech. Phys. Solids **103**, 236 (2017).

[19] R. Zhu, X. Liu, G. Hu, C. Sun, and G. Huang, Negative refraction of elastic waves at the deep-subwavelength scale in a single-phase metamaterial, Nat. Commun. **5**, 1 (2014).

[20] C. Shen, Y. Xie, N. Sui, W. Wang, S. A. Cummer, and Y. Jing, Broadband Acoustic Hyperbolic Metamaterial, Phys. Rev. Lett. **115**, 254301 (2015).

[21] V. M. García-Chocano, J. Christensen, and J. Sánchez-Dehesa, Negative Refraction and Energy Funneling by Hyperbolic Materials: An Experimental Demonstration in Acoustics, Phys. Rev. Lett. **112**, 144301 (2014).

[22] Z. Liang and J. Li, Extreme Acoustic Metamaterial by Coiling up Space, Phys. Rev. Lett. **108**, 114301 (2012).

[23] Z. Liang, T. Feng, S. Lok, F. Liu, K. B. Ng, C. H. Chan, J. Wang, S. Han, S. Lee, and J. Li, Space-coiling metamaterials with double negativity and conical dispersion, Sci. Rep. **3**, 1 (2013).

[24] Y. Xie, B.-I. Popa, L. Zigoneanu, and S. A. Cummer, Measurement of a Broadband Negative Index with Space-Coiling Acoustic Metamaterials, Phys. Rev. Lett. **110**, 175501 (2013).

[25] Y. Xie, W. Wang, H. Chen, A. Konneker, B.-I. Popa, and S. A. Cummer, Wavefront modulation and subwavelength diffractive acoustics with an acoustic metasurface, Nat. Commun. **5**, 1 (2014).

[26] B. Yuan, Y. Cheng, and X. Liu, Conversion of sound radiation pattern via gradient acoustic metasurface with space-coiling structure, Appl. Phys. Express **8**, 027301 (2015).

[27] C. Croënne, E.-D. Manga, B. Morvan, A. Tinel, B. Dubus, J. Vasseur, and A.-C. Hladky-Hennion, Negative refraction of longitudinal waves in a two-dimensional solid-solid phononic crystal, Phys. Rev. B **83**, 054301 (2011).

[28] A.-C. Hladky-Hennion, J. O. Vasseur, G. Haw, C. Croënne, L. Haumesser, and A. Norris, Negative refraction of acoustic waves using a foam-like metallic structure, Appl. Phys. Lett. **102**, 144103 (2013).

[29] J. Christensen and F. J. G. de Abajo, Anisotropic Metamaterials for Full Control of Acoustic Waves, Phys. Rev. Lett. **108**, 124301 (2012).

[30] L. Feng, X.-P. Liu, M.-H. Lu, Y.-B. Chen, Y.-F. Chen, Y.-W. Mao, J. Zi, Y.-Y. Zhu, S.-N. Zhu, and N.-B. Ming, Acoustic Backward-Wave Negative Refractions in the Second Band of a Sonic Crystal, Phys. Rev. Lett. **96**, 014301 (2006).

[31] I. Kourakis and P.-K. Shukla, Nonlinear propagation of electromagnetic waves in negative-refraction-index composite materials, Phys. Rev. E **72**, 016626 (2005).

[32] L. Fang, A. Mojahed, A. Darabi, A. F. Vakakis, and M. J. Leamy, Passive Nonreciprocity in a System of Asymmetrical Rotational Oscillators, Phys. Rev. Appl. **15**, 034005 (2021).

[33] L. Fang and M. Leamy, Harnessing rotational geometry to design reconfigurable dispersion and refractive index in nonlinear acoustic metamaterials, J. Acoust. Soc. Am. **151**, A39 (2022).

[34] P. Wang, L. Lu, and K. Bertoldi, Topological Phononic Crystals with One-Way Elastic Edge Waves, Phys. Rev. Lett. **115**, 104302 (2015).

[35] M. Attarzadeh, S. Maleki, J. Crassidis, and M. Nouh, Non-reciprocal wave phenomena in energy self-reliant gyric metamaterials, J. Acoust. Soc. Am. **146**, 789 (2019).

[36] L. M. Nash, D. Kleckner, A. Read, V. Vitelli, A. M. Turner, and W. T. Irvine, Topological mechanics of gyroscopic metamaterials, Proc. Nat. Acad. Sci. **112**, 14495 (2015).

[37] Y. Alsaffar, S. Sassi, and A. Baz, Band gap characteristics of periodic gyroscopic systems, J. Sound Vib. **435**, 301 (2018).

[38] M. A. Attarzadeh, J. Callanan, and M. Nouh, Experimental Observation of Nonreciprocal Waves in a Resonant

Metamaterial Beam, Phys. Rev. Appl. **13**, 021001(R) (2020).

[39] M. I. Hussein, M. J. Leamy, and M. Ruzzene, Dynamics of phononic materials and structures: Historical origins, recent progress, and future outlook, Appl. Mech. Rev. **66**, 040802 (2014).

[40] L. Fang, A. Darabi, A. Mojahed, A. F. Vakakis, and M. J. Leamy, Broadband non-reciprocity with robust signal integrity in a triangle-shaped nonlinear 1D metamaterial, Nonlinear Dyn. **100**, 1 (2020).

[41] C. J. Adkins, Phonons near interfaces, J. Phys. Condens. Matter. **2**, 1445 (1990).

[42] M. D. Fronk and M. J. Leamy, Higher-order dispersion, stability, and waveform invariance in nonlinear monoatomic and diatomic systems, J. Vib. Acoust. **139**, 051003 (2017).

[43] K. Manktelow, M. J. Leamy, and M. Ruzzene, Multiple scales analysis of wave–wave interactions in a cubically nonlinear monoatomic chain, Nonlinear Dyn. **63**, 193 (2011).

[44] A. H. Nayfeh, *Perturbation Methods* (John Wiley & Sons, Weinheim, Germany, 2008).

[45] L. Fang and M. J. Leamy, Perturbation analysis of nonlinear evanescent waves in a one-dimensional monatomic chain, Phys. Rev. E **105**, 014203 (2022).

[46] W. Jiao and S. Gonella, Wavenumber-space band clipping in nonlinear periodic structures, Proc. R. Soc. A **477**, 20210052 (2021).